Geomechanics and Engineering, *Vol. 13, No. 5 (2017) 715-742*
DOI: https://doi.org/10.12989/gae.2017.13.5.715

Numerical and experimental study of multi-bench retained excavations

Gang Zheng[1,2], Dongqing Nie[1,2], Yu Diao[1,2], Jie Liu[1,2] and Xuesong Cheng[*1,2]

[1]*MOE Key Laboratory of Coast Civil Structure Safety, Tianjin University, 92 Weijin Rd., Nankai District, Tianjin 300072, China*
[2]*Department of Civil Engineering, Tianjin University, 92 Weijin Rd., Nankai District, Tianjin 300072, China*

(*Received August 20, 2017, Revised April 28, 2017, Accepted May 11, 2017*)

Abstract. Earth berms are often left in place to support retaining walls or piles in order to eliminate horizontal struts in excavations of soft soil areas. However, if the excavation depth is relatively large, an earth berm-supported retaining system may not be applicable and could be replaced by a multi-bench retaining system. However, studies on multi-bench retaining systems are limited. The goal of this investigation is to study the deformation characteristics, internal forces and interaction mechanisms of the retaining structures in a multi-bench retaining system and the failure modes of this retaining system. Therefore, a series of model tests of a two-bench retaining system was designed and conducted, and corresponding finite difference simulations were developed to back-analyze the model tests and for further analysis. The tests and numerical results show that the distance between the two rows of retaining piles (bench width) and their embedded lengths can significantly influence the relative movement between the piles; this relative movement determines the horizontal stress distribution in the soil between the two rows of piles (i.e., the bench zone) and thus determines the bending moments in the retaining piles. As the bench width increases, the deformations and bending moments in the retaining piles decrease, while the excavation stability increases. If the second retaining piles are longer than a certain length, they will experience a larger bending moment than the first retaining piles and become the primary retaining structure. In addition, for varying bench widths, the slip surface formation differs, and the failure modes of two-bench retained excavations can be divided into three types: integrated failure, interactive failure and disconnected failure.

Keywords: multi-bench retained excavation; model test; finite difference method; strain softening; failure mechanism; earth berm

1. Introduction

With the rapid development of urban areas and increasing urban populations, exploiting the underground spaces of cities is an urgent need. Recently, the construction scale of excavation projects has become increasingly large. The plan area of an excavation could be several hundred thousand square meters for the construction of multi-purpose building groups or large transportation centers.

A large and very deep excavation in a soft soil area typically uses a support system consisting

*Corresponding author, Ph.D., E-mail: cheng_xuesong@163.com

http://www.techno-press.org/?journal=gae&subpage=7 ISSN: 2005-307X (Print), 2092-6219 (Online)

of a retaining wall or pile and one or more levels of horizontal struts. The shortcomings of this type of retaining system are notable: horizontal strut systems are costly and require a long construction period (Yang *et al*. 2006); the space allotted for soil excavation and basement construction is limited; and because the horizontal struts have to be dismantled after completing the basement, the abandoned struts cause problems and are not environmentally friendly (Park *et al*. 2009).

To eliminate horizontal struts, berm-supported retaining walls or piles can be used, as shown in Fig. 1(a). The finite element method has been used for parametric studies on this approach (Carder and Bennett 1996, Clough and Davidson 1977, Georgiadis and Anagnostopoulos 1998, Gourvenec and Powrie 2000, Potts *et al*. 1993), and centrifuge model tests have been used to study the factors that can influence the behavior of berm-supported walls (Powrie and Daly 2002). Furthermore, various methods for analyzing earth berms have been proposed. Daly and Powrie (2001) proposed a modified limit-equilibrium analysis approach to provide a reasonable estimate of the lateral stresses exerted by the berm on the retaining walls or piles and compared the results with those of several limit-equilibrium analysis methods.

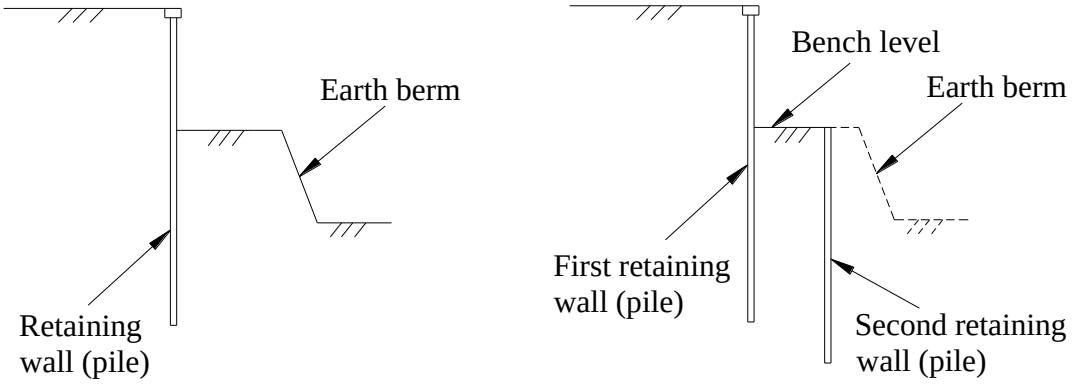

(a) Berm-supported retaining system (b) Multi-bench retaining system

Fig. 1 Comparison of the berm-supported retaining system and the multi-bench retaining system

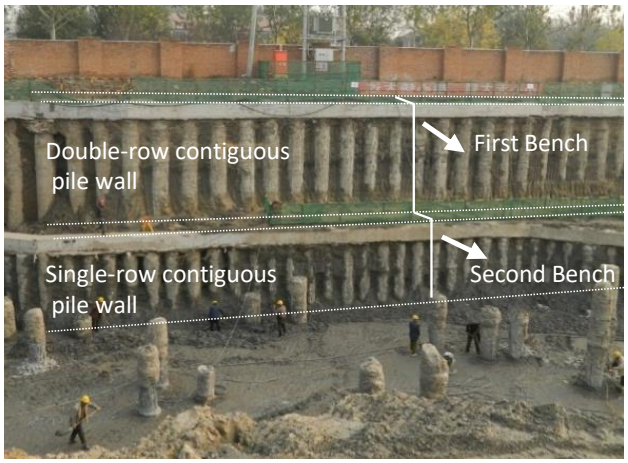

Fig. 2 Photograph of an example two-bench excavation supported by contiguous bored pile walls

However, an earth berm-supported retaining structure is generally not suitable for excavations with considerable depth (greater than approximately 10 m), in these cases, the failure probability will be quite high if the earth berm is not sufficiently improved (Liao and Lin 2009). Moreover, berms occupy a large area when the excavation depth is relatively large. For excavations with greater depths or with insufficient space for earth berms, an extra row of piles or an extra wall can be constructed in the berm to establish a multi-bench retaining system, as shown in Fig. 1. In this retaining system, different types of retaining structures, such as single-row piles or a retaining wall (Bolton and Powrie 1987, Ouria *et al*. 2016), double-row piles (Lee *et al*. 2011), a sheet pile retaining wall (Qu *et al*. 2016), gravity retaining walls, or batter piles (Seo *et al*. 2016) can be used for each row of the retaining structure. The range of excavation depth can vary from 10 m to 20 m when using different combinations of retaining structures in a two-bench retaining system. Furthermore, if three or four benches are used, a much greater excavation depth can be achieved.

Recently, several ultra-large excavations in the soft ground of Tianjin, China, have been successfully completed using the multi-bench excavation technique. The multi-bench retaining system is economical and time-saving compared to a strutted retaining system. For instance, a basement excavation project in Tianjin with a plan area of 7800 m^2 and an excavation depth of 14.5 m was successfully completed using a two-bench retaining system, as shown in Fig. 2. The excavation was step-shaped and consisted of two levels: the first bench and the second bench. Double-row and single-row contiguous pile walls were used as the first and second retaining structures, respectively. The cost of the multi-bench retaining system was 38 million RMB less than that of the original design scheme, which consisted of a retaining wall and two levels of horizontal struts. Moreover, the excavation and basement construction were completed 3 months earlier than indicated by the original plan due to the use of the multi-bench retaining system.

Although the multi-bench retaining system has been used in several deep and large excavations, research on this method is still limited. To investigate the working and failure mechanisms of the multi-bench retaining system and to study the impacts of its geometric parameters, a series of 1-g plane-strain model tests were conducted in a test platform built by the researchers. Then, two-dimensional (2D) models were established using the finite difference method (FDM) to verify the model test results and to gain a better understanding of the retaining system.

2. Scope and objective

The objective of this paper is to investigate the performance and the failure mechanism of a new excavation retaining system, i.e., a multi-bench retaining system. A series of model tests and numerical simulations was conducted to study the deformation characteristics, internal forces and interaction mechanisms of the retaining structures in a multi-bench retaining system. The earth pressures of the bench zone acting on the retaining structures were analyzed to better understand the interaction mechanism of the retaining structures in a multi-bench retaining system. In conventional geotechnical engineering, defining the failure mechanism is the basis for establishing the stability analysis method. Therefore, the failure modes of the multi-bench retained excavation were determined based on experimental and numerical results. In addition, the influences of the geometric parameters of the system, such as the bench width and the length of the second retaining pile, on the performance and failure mechanism of the retaining system were also investigated. Additionally, to determine the advantages of this new retaining system, the deformations and bending moments of the piles in a multi-bench retaining system were compared with those of a

traditional cantilever retaining structure. This study can provide a reference for establishing the design and stability evaluation methods for multi-bench retaining systems.

3. Model test introduction

3.1 Experimental setup

Model tests in the 1-g condition, which are widely used in geotechnical research (Bildik and Laman 2015, Kim *et al.* 2012), were adopted in this study. The test platform consisted of a sand raining device and a sand tank, as shown in Fig. 3. The sand tank was constructed using masonry covered by cement sand plaster and had inner dimensions of 2.50 m×2.46 m×1.40 m (length× width×height). Two toughened glass windows were installed on two sides of the sand tank to observe the deformation of the soil inside. Except for the observation windows, the walls of the sand tank were covered with Teflon membranes to eliminate friction between the wall and soil.

As shown in Fig. 3, the sand raining equipment was installed above the soil tank. The sandbox was 2.46 m long and bridged the width of the tank. The cross-section of the sandbox was funnel-shaped, and the exit of the sandbox was a long, thin opening (2.46 m×5 mm) located 1.7 m above the bottom of the tank. During the sand raining process, the sandbox moved backward and forward on steel rails along the length of the tank at a constant rate to pour the sand into the tank in a uniform manner. The model piles were installed as soon as the sand reached the bottom of these piles.

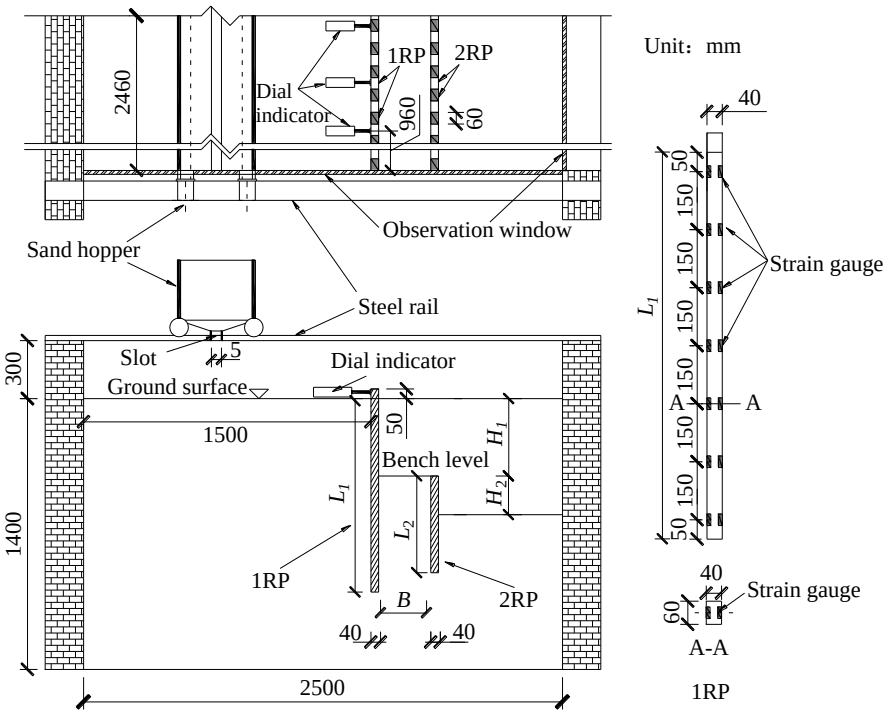

Fig. 3 Schematic of the model test (units: mm)

Table 1 Geometric parameters for each test

Test number	L_1 (mm)	L_2 (mm)	B (mm)	H_1 (mm)	H_2 (mm)
M1	1000	500	100	400	300
M2	1000	500	200	400	300
M3	1000	500	400	400	300
M4	1000	700	100	400	300

Table 2 Parameters of the sand derived from laboratory tests

Laboratory test parameter	Dry density ρ (kg/m^3)	Mean grain size d_{50} (mm)	Coefficient of nonuniformity Cu	Maximum void ratio e_{max}	Minimum void ratio e_{min}	Specific gravity Gs	Critical friction angle φ_{res}^{DS} (°)	Peak friction angle φ_p^{DS} (°)	Peak dilation angle ψ_p (°)
Value	1600	0.20	2.25	0.85	0.43	2.67	31	35	8.3

3.2 Test information

Four model tests with varying bench widths (B) and lengths of the second retaining pile (L_2) were conducted. The profile of the model test is shown in Fig. 3. A two-bench excavation retained by two rows of single-row contiguous pile walls was investigated in these tests. The total normal excavation depth was 700 mm: the first excavation depth H_1 was 400 mm, and the second excavation depth H_2 was 300 mm. The bottom of the first excavation, i.e., the top level of the second bench, is called the bench level in the following sections, as shown in Fig. 3. The normal excavation was conducted in 7 stages, with a depth of 100 mm for each stage. After the normal excavation reached 700 mm, excavation continued until the retaining system failed. The distance between the first retaining piles and the boundary of the sand tank was 1500 mm, which was more than 2 times the greatest excavation depth (750 mm) and was larger than the influence range of the excavation in sand (Peck 1969).

The model piles were made of polyvinyl chloride (PVC) pipes with a sectional flexural rigidity (EI) of 560 N·m^2 (as measured via loading tests). The outer cross-sectional dimensions of the model pile were 60 mm×40 mm (Fig. 3), and the thickness of the pipe wall was approximately 3 mm. The length of the first retaining piles (1RP) and the second retaining piles (2RP) were 1000 mm and 500 mm (700 m in Test 4), respectively. The details of the main geometric parameters for each test are shown in Table 1.

3.3 Model preparation

Dry fine sand was used in these tests, and the physical and mechanical properties of this sand were measured by laboratory tests. According to the test results, this sand had a mean grain size (d_{50}) of 0.20 mm and a specific gravity (Gs) of 2.67. The sand models were prepared using the pluvial deposition method. As the hopper could only move along the length of the sand tank, the falling height of the sand gradually changed from 1700 mm to 300 mm during the preparation process, and the corresponding void ratio and density varied from 0.62 to 0.76 and 1650 to 1520 kg/m^3, respectively. At the middle height of the model, the void ratio was approximately 0.67, and the corresponding density was 1600 kg/m^3. The details of the main sand parameters are shown in

Table 2, and the parameters derived from the direct shear tests were based on the sand sample at the middle height of the model.

3.4 Instrumentation

As shown in Fig. 3, the horizontal displacements at the heads of the three 1RP were monitored using dial indicators. To obtain the bending moment of the 1RP, a series of miniature strain gauges were symmetrically mounted on the tensile and compressive sides of the inner wall of the model pile to form half Wheatstone bridges to compensate for any temperature effects. The strain gauges were installed along the length of the pile at a spacing of 150 mm. All instrumentation devices were arranged in the central part of a row of retaining piles to avoid boundary effects.

4. Numerical model introduction

Because the data derived from the model tests were relatively limited, a numerical back analysis was conducted using a FDM software, namely, FLAC 3D 5.0, to improve the understanding of the multi-bench retaining system. The numerical results were compared with and used to supplement the model test results.

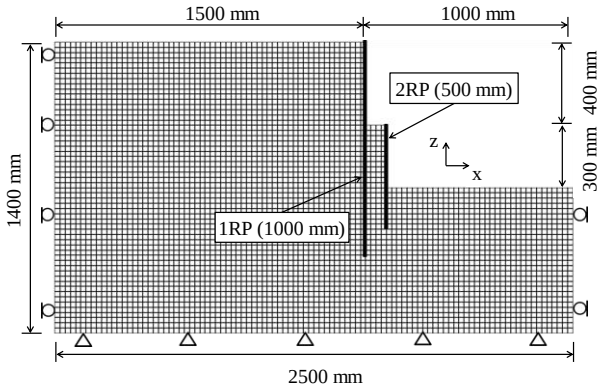

(a) FDM model of M1

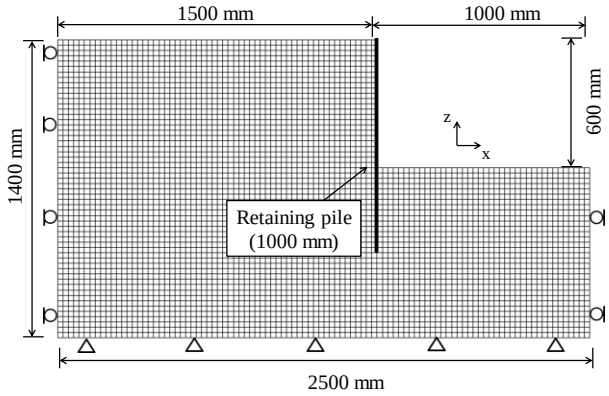

(b) Single-row pile model

Fig. 4 Finite difference mesh and boundary conditions

4.1 Mesh and boundary conditions of the numerical model

A typical finite difference model mesh with boundary conditions is shown in Fig. 4(a), taking M1 with an excavation depth of 700 mm as an example. A 2D finite difference model was used because the sand tank was sufficiently wide to ensure that the middle part of the retaining structure satisfied the plane strain assumption. The numerical model dimensions in the x and z directions were equal to those of the model test profile, which were 2500 mm long and 1400 mm high. The left and right boundaries of the numerical model were fixed with roller supports, and the bottom boundary was fixed with pin supports. The soil was modeled using 8-node solid elements.

In addition to the FDM models of M1-M4, another finite difference model was established to simulate the excavation retained by only one row of retaining piles (with a pile length of 1000 mm) for comparison, as shown in Fig. 4(b). This model is called a single-row pile model in the following sections.

In the numerical simulations, the excavation depth in each step was 100 mm, which was equal to that in the model tests. After the excavation reached a depth of 700 mm, the additional excavation depth in each step was 25 mm, and excavation continued until the numerical calculation could not converge. The last excavation depth at which the numerical simulation could converge was considered the critical depth.

4.2 Constitutive models and soil parameters

The application of the advanced soil model is important in numerical analysis (Ardakani *et al*. 2014). The Cap-Yield (CYsoil) Model, a built-in constitutive model in FLAC 3D, was used to simulate the fine sand in the model tests. The CYsoil model is a strain-hardening constitutive model characterized by a frictional Mohr-Coulomb shear envelope (zero cohesion) and an elliptical volumetric cap, for which the ratio of the axes lengths is defined by the shape parameter, α. The basic CYsoil model behavior can be enhanced using three types of hardening laws: a cap-hardening law, a friction-hardening law and a compaction/dilation law (Itasca Consulting Group 2009). This constitutive model is suitable for predicting soil behavior in tunnel engineering (Do *et al*. 2013a, b) and excavation engineering (Itasca Consulting Group 2009).

In this study, a direct shear device was used to obtain the friction and dilation angles of the sand. In the direct shear tests, the sand showed strain softening, which significantly impacted its deformation and shear band propagation (Anastasopoulos *et al*. 2007). Therefore, the strain softening characteristic was introduced into the CYsoil model by changing the mobilized friction angle and the mobilized dilation angle with increasing plastic shear strain, as shown in Fig. 5. The plastic shear strain at the peak mobilized friction angle, γ^{p}_{p}, and that at the end of softening, γ^{p}_{f}, can be obtained from the direct shear test results. The conversion formulas are represented by Eqs. (1) and (2) (Anastasopoulos *et al*. 2007).

$$\gamma_{\mathrm{p}}^{\mathrm{p}} = \frac{\delta x_{\mathrm{p}} - \delta x_{\mathrm{y}}}{D} \tag{1}$$

$$\gamma_{\mathrm{f}}^{\mathrm{p}} = \gamma_{\mathrm{p}}^{\mathrm{p}} + \frac{\delta x_{\mathrm{f}} - \delta x_{\mathrm{p}}}{d_B} = \frac{\delta x_{\mathrm{p}} - \delta x_{\mathrm{y}}}{D} + \frac{\delta x_{\mathrm{f}} - \delta x_{\mathrm{p}}}{16 d_{50}} \tag{2}$$

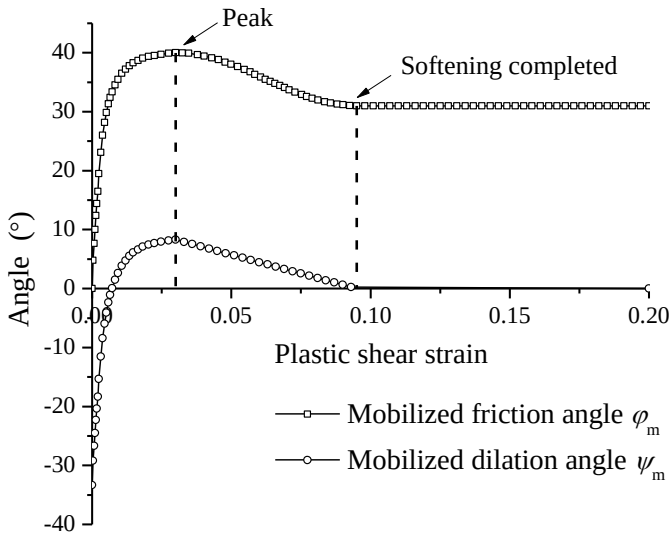

Fig. 5 Modified friction and dilation angle versus the plastic shear strain

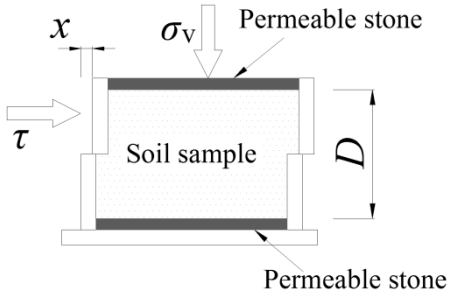

Fig. 6 Sketch of the direct shear test

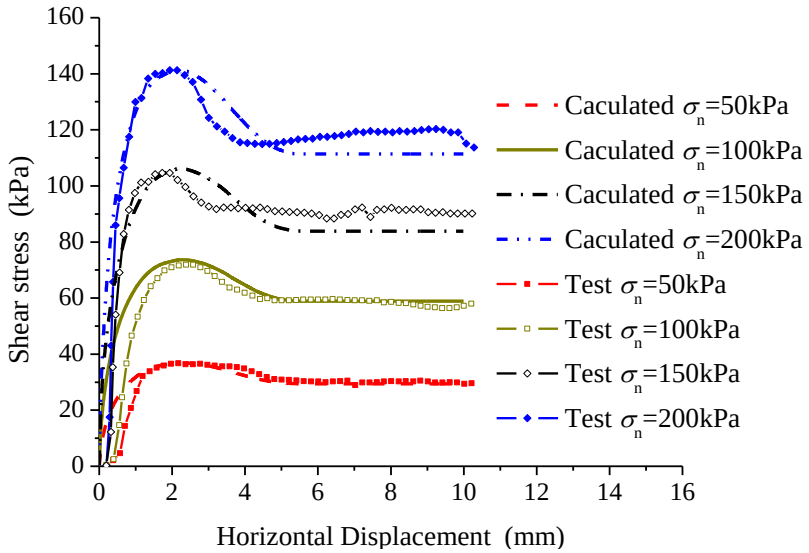

Fig. 7 Comparison between the results of the direct shear tests and the FDM analysis

Table 3 The model sand properties

CYsoil model parameter	Dry density ρ (kg/m^3)	Reference elastic tangent shear modulus G^e_{ref} (MPa)	Reference effective pressure p_{ref} (kPa)	Failure ratio R_f *	Cap-yield surface parameter α	Peak friction angle φ_p (°)	Ultimate friction angle φ_f (°)	Peak dilation angle ψ_p (°)	Poisson's ratio v
Value	1600	80.8	100	0.9	1	40	31	8.3	0.3

*R_f is a constant that is less than 1 (0.9 in most cases) and is used to assign a lower bound for G_p, which is the plastic shear modulus (Itasca Consulting Group 2009)

where δx_y, δx_p and δx_f are the horizontal displacement before plastic behavior, at the peak mobilized friction angle and at the completion of softening in the direct shear test, respectively; D is the thickness of the soil sample in the direct shear test, as shown in Fig. 6; d_B is the width of the shear band in the direct shear test after the end of softening; and d_{50} is the mean grain size of the sand. All plastic shear deformation is assumed to takes place within the shear band, which is equal to $16d_{50}$ as proposed by Vardoulakis and Graf (1985).

The analysis results from the finite element simulation using a constitutive model with strain softening are mesh dependent (Pietruszczak and Mróz 1981), which is also believed to be true for the FDM results. The approximate simplified scaling method presented by Anastasopoulos *et al*. (2007) is adopted in this paper. In this method, the plastic shear strain at which softening is completed, γ^p_f, is replaced by $\gamma^p_{f,FDM}$ in the FDM analysis, and the conversion formula is presented in Eq. (3).

$$\gamma^p_{f,FDM} = \gamma^p_p + \frac{\delta x_f - \delta x_p}{16d_{50}} \frac{16d_{50}}{d_{FDM}} = \frac{\delta x_p - \delta x_y}{D} + \frac{\delta x_f - \delta x_p}{d_{FDM}} \tag{3}$$

where d_{FDM} is the side length of a mesh element. Scaling is not applied to the parameter γ^p_p because the shear band width is assumed to be equal to D before the end of softening (Anastasopoulos *et al*. 2007). In this way, scale can be approximately incorporated into the FDM model. As the plain strain assumption is adopted in this FDM analysis, the plane strain peak friction angle, φ_p, can be calculated using Eq. (4) (Jewell 1989).

$$\sin\varphi_p = \frac{\tan\varphi_p^{DS}}{\cos\psi_p + \sin\psi_p \tan\varphi_p^{DS}} \tag{4}$$

where φ_p^{DS} is the peak friction angle obtained by a direct shear test and ψ_p is the peak dilation angle. Based on the direct shear test results, φ_p^{DS} is 35.0°, and ψ_p is 8.3°; therefore, the corrected peak friction angle, φ_p, is 40.0°.

To verify the applicability of this constitutive model, the direct shear tests were simulated, and the calculated and experimental test results are shown in Fig. 7. The calculated curves match the test results well.

Another issue is that the stress level in 1-g model tests is quite low, i.e., the mean principle stress is lower than 50 kPa, and laboratory tests are difficult to conduct at low pressures. Tatsuoka

et al. (1986) noted that the changes in the strength and deformation characteristics of sand are very small when the confining pressure (σ_3') is less than 50 kPa. Therefore, laboratory tests at a normal stress level are used to estimate the strength and deformation characteristics of the sand. The main properties of the sand used in the numerical analysis are summarized in Table 3.

4.3 Model pile parameters

The model piles were simulated by linear elements with interfaces on both sides. Based on the equivalent flexural stiffness method, the Young's modulus and the equivalent thickness of the pile were determined to be 1.9 GPa and 40 mm, respectively. The density of the model pile was neglected in this study.

The hardening and softening behavior of soil and the soil-structure interface is an important feature for accurate modelling. Anastasopoulos *et al*. (2007) adopted an elasto-plastic Mohr-Coulomb constitutive model with isotropic strain softening to study fault rupture propagation through sand. Desai and Ma (1992) proposed a unified constitutive model based on the disturbed state concept (DSC) for the static behavior of rock joints and interfaces, which allows for the hardening and softening response of joints. The hierarchical single-surface (HISS) plasticity model, which can allow for isotropic and anisotropic hardening of solids, can accurately predict the behavior of fiber-reinforced polymer and backfill soil interface (Toufigh *et al.* 2014). The HISS plasticity model with DSC has also been used to predict the softening behavior of polymer/ordinary concrete and sand interfaces, and the model results were in good agreement with results from direct shear tests (Toufigh *et al.* 2016).

Due to the limitations of the software used for the numerical simulation in this paper (Itasca Consulting Group 2009), a relatively simple interface characterized by Coulomb sliding was adopted to model the soil-pile interface. According to the direct shear test, the friction angle between the model pile and the sand was 16°. The normal and shear stiffnesses of the interface (K_n and K_s) are approximately ten times the equivalent stiffness of the stiffest neighboring zone and can be expressed by Eq. (5) (Itasca Consulting Group 2009).

$$K_n = K_s = 10 \times \max\left[\frac{\left(K + \frac{4}{3}G\right)}{\Delta z_{\min}}\right] \tag{5}$$

where K and G are the bulk and shear moduli of the soil, respectively, and $\Delta z_{\min}$ is the smallest width of an adjoining zone in the normal direction of the interface.

5. Measured and computed results

5.1 Horizontal pile displacement

5.1.1 Horizontal displacement at the pile head

Fig. 8 shows the curves of the horizontal displacement at the heads of the 1RP varying with excavation depth for different tests. The calculated pile displacements match the test results well, which preliminarily verifies the accuracy of both the FDM simulation and the model test.

After reaching an excavation depth of 650 mm, the single-row pile model could not converge; therefore, its displacement at 700 mm is not shown in Fig. 8. The ultimate excavation depths in the multi-bench excavations (M1-M4) were larger than that in the single-row pile model, preliminarily verifying the efficiency of the multi-bench retaining system.

For the first excavation phase, the calculated displacements in M1-M4 were smaller than that in the single-row pile model. This result implies that adding the 2RP improved the passive resistance of the soil below the bench level (Hong and Ng 2013). The effect of the reinforcement on the passive resistance decreased with increasing B; therefore, the horizontal displacement of the 1RP increased with increasing B. In addition, the horizontal displacement of the 1RP decreased with increasing L_2, which means that increasing L_2 improves the effect of the reinforcement on the passive resistance.

For the second excavation phase, the slopes of the curves for M1-M4 were slightly smaller than that in the single-row pile model. The calculated displacements in M1-M4 were 22.6%, 36.8%, 54.6% and 37.9% smaller than that of the single-row pile model at an excavation depth of 600 mm, respectively. As the excavation depth increased, the horizontal displacement of the 2RP increased rapidly; therefore, the soil between the two rows of piles and under the bench level (i.e., the bench zone soil) was loosened. Consequently, the increasing rate of the horizontal displacement of the 1RP gradually increased in the second excavation phase for M1-M4. Because the influence of the displacement of the 2RP on the 1RP decreased with increasing B in the second excavation phase, unlike in the first excavation phase, the horizontal displacement of the 1RP deceased with increasing B but still decreased as L_2 increased. For example, the horizontal displacements of the 1RP in M3 and M4 were 69.3% and 46.5% smaller than that in M1 at an excavation depth of 700 mm, respectively.

The displacements at the heads of the 2RP mostly developed during the second excavation phase, and these displacements had a similar characteristic to those of the 1RP. Therefore, the displacements of the 2RP are not discussed in detail here.

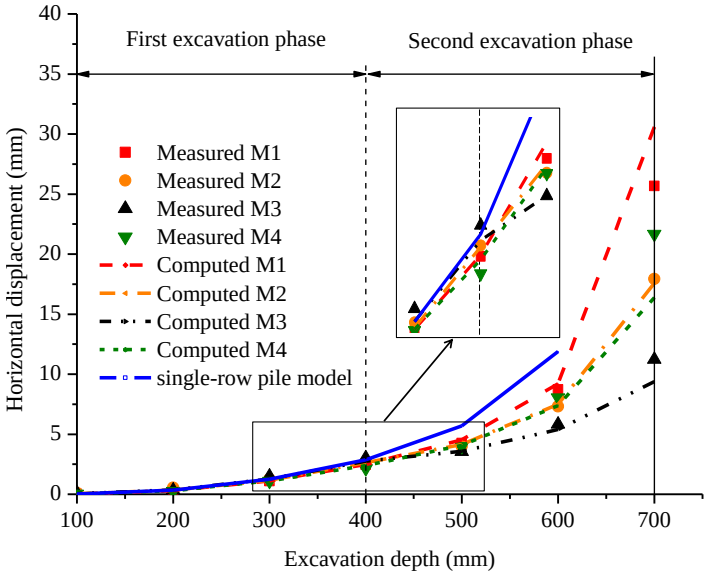

Fig. 8 The horizontal displacement at the 1RP crest

5.1.2 Lateral deflections of the pile shafts

The calculated lateral deflections of the 1RP and 2RP for M1-M4 are shown in Fig. 9. For excavation depths of 400 mm and 600 mm in M1-M3, the lateral deflections of the 2RP are smaller than those at the corresponding heights of the 1RP. This finding indicates that the entire bench zone was compacted, and this compacted bench zone is called the "compaction zone". For instance, for an excavation depth of 600 mm in M1, the lateral deflection of the 1RP at 400 mm below ground surface (BGS) was 0.4 mm larger than that of the 2RP; however, the differences between the 1RP and 2RP deflections for M2 and M3 at 400 mm BGS were 0.7 mm and 0.8 mm, respectively. The values of B in M1, M2 and M3 were 100 mm, 200 mm and 400 mm, respectively. Therefore, the compaction ratio (defined as the ratio of the difference between the deflections of the 1RP and 2RP over B) decreases with increasing B.

For an excavation depth of 700 mm for M1-M3, the lateral deflections of the upper portion of the 2RP (approximately 400 mm-700 mm BGS) were larger than those at the corresponding heights of the 1RP, whereas the lateral deflections of the lower portion of the 2RP (approximately 700 mm-900 mm BGS) were smaller than those at the corresponding heights of the 1RP. Therefore, the upper portion of the bench zone soil was compacted (compaction zone), whereas the lower portion was relaxed. The area of the relaxed bench zone is called the "relaxation zone". The boundary between the compaction and relaxation zones at the excavation depth of 700 mm in each test is represented by the dashed-dotted lines in Fig. 9.

Fig. 9(d) shows the lateral deflections of the piles in M4. At an excavation depth of 400 mm, the soil in the bench zone was compacted. At excavation depths of 600 mm and 700 mm, the upper portion of the bench zone soil was relaxed, and the lower portion was compacted. The boundaries were located at approximately 900 mm and 700 mm BGS for excavation depths of 600 mm and 700 mm, respectively.

The horizontal stress distribution in the bench zone is closely related to the compacted or relaxed state of the soil (the relative movement between the two rows of piles), as discussed in Section 4.2. The displacements at the pile toes were not zero. The soil state (compacted or relaxed) is the combined result of the translational displacements and rotations of the two rows of piles. Furthermore, the relative movement characteristics between the two rows of the piles were primarily determined by the embedded pile lengths.

The compaction and relaxation zones in M1 and M4 were located at opposite positions for an excavation depth of 700 mm; this result was primarily caused by different relative rotation angles between the 1RP and 2RP. The rotation angle of the 2RP was larger than that of the 1RP in M1 because the embedded length of the 2RP was relatively small. Therefore, the upper part of the bench zone was relaxed, and the lower part was compacted. In contrast, the rotation angle of the 1RP was larger than that of the 2RP in M4 because the embedded length of the 2RP in M4 was much larger than that in M1. Therefore, the relaxation zone and the compaction zone in M4 were located at opposite positions of those in M1.

5.2 Earth pressure

In a two-bench retaining system, the earth pressures acting on the retained side of the 1RP tended toward the active state, while those on the excavated side of the 2RP tended toward the passive state. However, the stress state of the soil between the two rows of retaining piles is difficult to determine when B is relatively small because the conventional earth pressure analysis methods are inapplicable to this limited soil mass. However, knowing the stress state of the soil

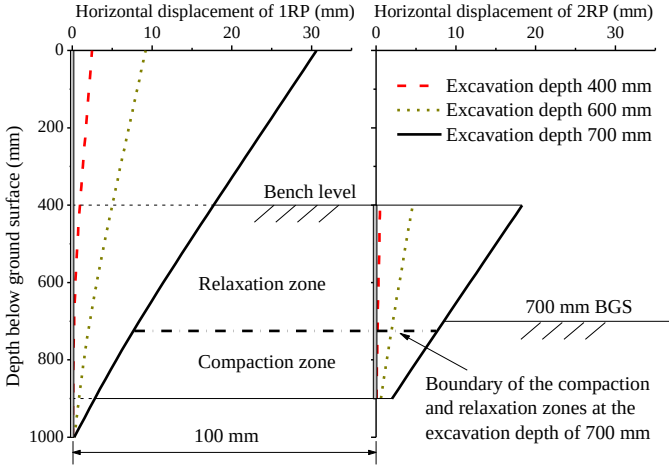

(a) M1

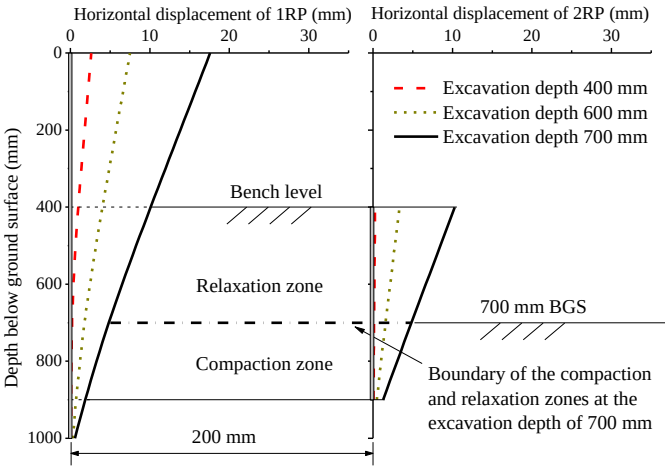

(b) M2

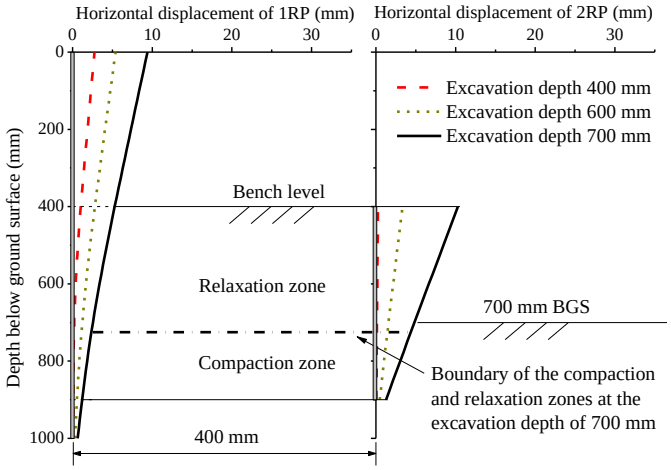

(c) M3

Fig. 9 Lateral deflections of the 1RP and 2RP

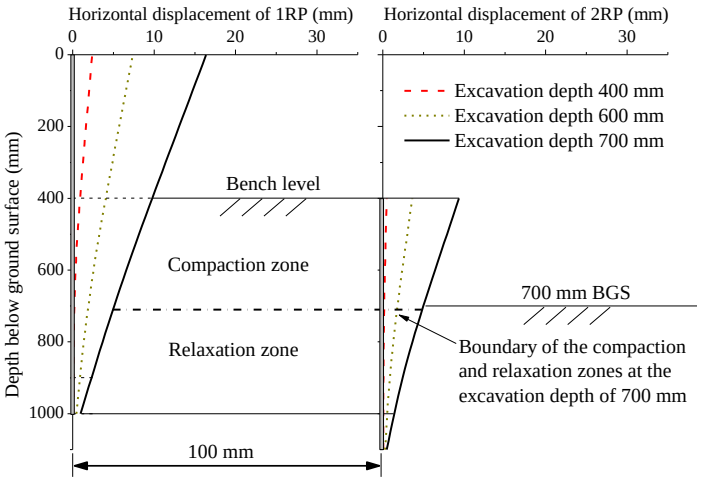

(d) M4

Fig. 9 Continued

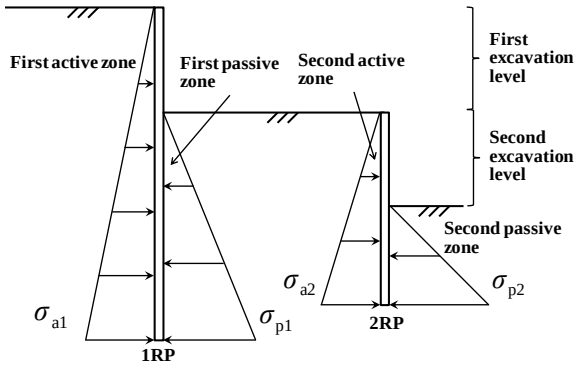

Fig. 10 Earth pressure zones in a multi-bench excavation

between the two rows of retaining piles is crucial for determining the behavior of a two-bench retaining system; therefore, this is the primary focus of this study.

Studies on the earth pressures acting on retaining walls or piles by narrow backfills have been conducted by many researchers. Several research methods have been used, such as centrifuge tests (Frydman and Keissar 1987, Take and Valsangkar 2001), numerical simulations (Fan and Fang 2010, Yang and Liu 2007), and analytical methods (Greco 2013, Zhao and Zhu 2014). The above studies mainly focused on the earth pressure exerted by the limited soil mass between a removable vertical boundary and a fixed vertical boundary. However, in a two-bench retained excavation, both vertical boundaries of the soil between the two rows of retaining piles are removable and flexible.

For convenience, the soil zones on the left and right sides of the 1RP are defined as the first active zone and the first passive zone, respectively, as shown in Fig. 10. Similarly, the soil zones on the left and right sides of the 2RP are defined as the second active zone and the second passive zone, respectively. However, the first passive zone and the second active zone cannot be rigorously separated. The symbols σ_{a1} and σ_{p1}, as shown in Fig. 10, are the earth pressures acting on the active

and passive sides of the 1RP, respectively, and σ_{a2} and σ_{p2} are the earth pressures acting on the active and passive sides of the 2RP, respectively.

According to Bolton and Powrie (1987), an unpropped wall will fail as a rigid body by rotating about an axis along the wall at a distance z_p below the bottom of the excavation. Figs. 11-14 show that the calculated earth pressures σ_{a1} and σ_{p2} in the two-bench retained excavations at the critical state have the same pattern as the stress distribution of an unpropped wall, as proposed by Bolton and Powrie (1988).

The lateral earth pressures exerted by the soil mass between the two rows of piles, i.e., σ_{a2} and σ_{p1}, for M1, M2, M3, and M4 are shown in Figs. 11-14, respectively. In these figures, the bench level is 400 mm BGS. These figures show the earth pressures for excavation depths of 400 mm, 500 mm, 600 mm, 700 mm and the critical excavation depth (i.e., 700 mm, 725 mm, 750 mm and 750 mm for M1, M2, M3, and M4, respectively).

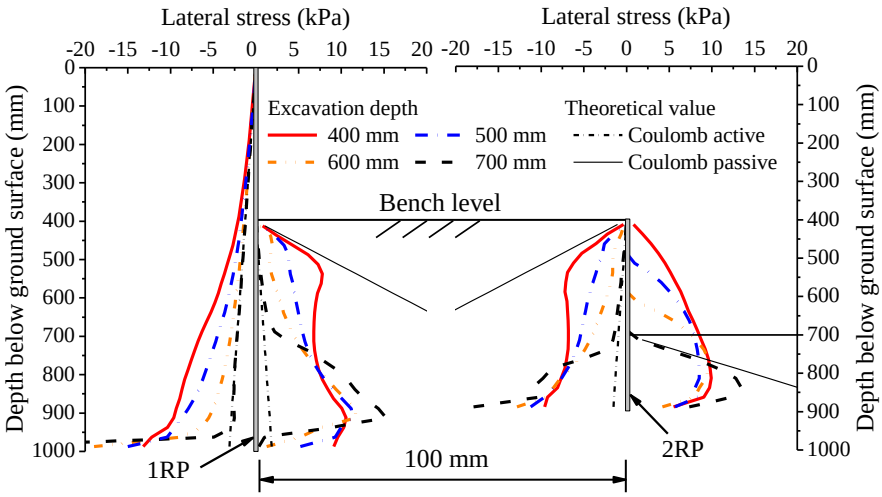

Fig. 11 Lateral earth pressures for M1

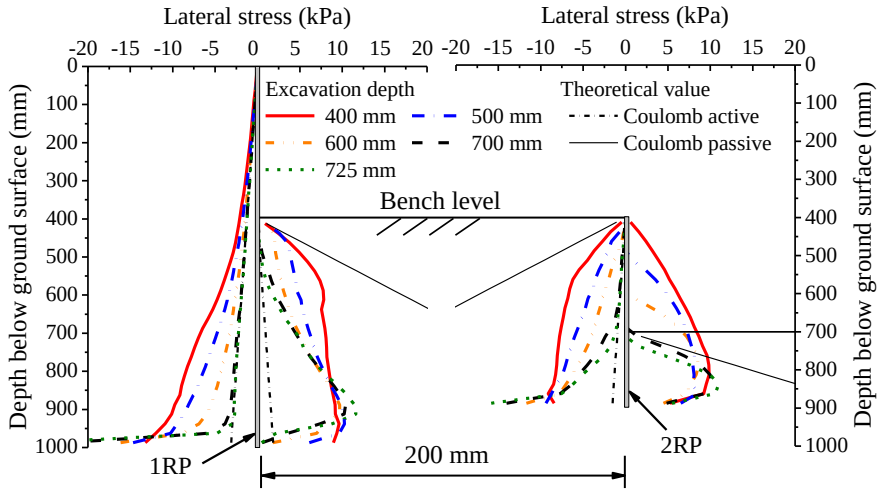

Fig. 12 Lateral earth pressures for M2

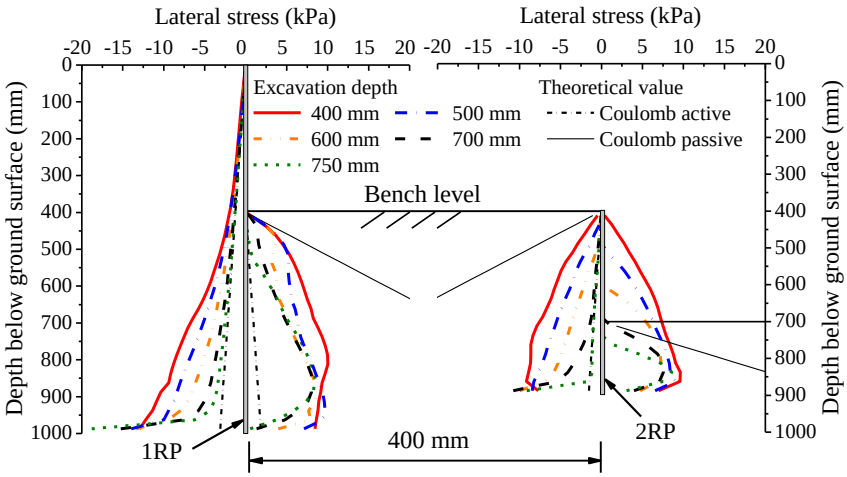

Fig. 13 Lateral earth pressures for M3

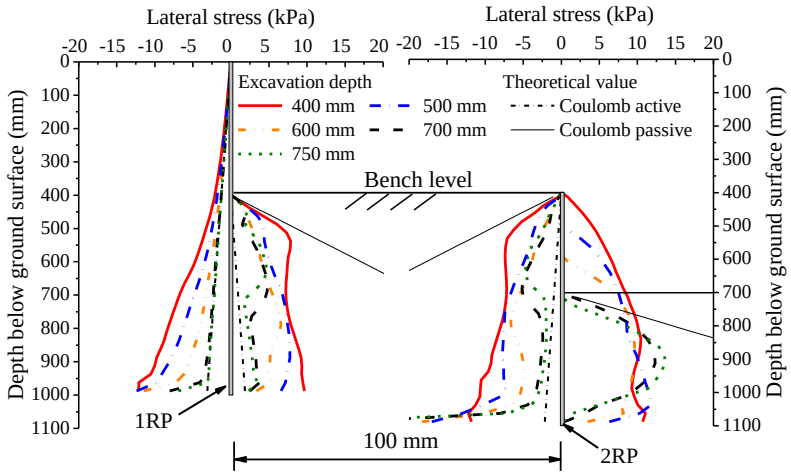

Fig. 14 Lateral earth pressures for M4

5.2.1 Analysis of M1

For M1 (Fig. 11), when the first excavation phase was completed (400 mm), the earth pressure distributions of σ_{p1} and σ_{a2} had similar shapes and magnitudes. The earth pressures (σ_{p1} and σ_{a2}) between 400 mm and 550 mm BGS were close to the Coulomb passive pressure, whereas the earth pressures between 550 mm and 1000 mm BGS (900 mm for the 2RP) exhibited a bow shape.

When the retaining system approached the critical state (i.e., an excavation depth of 700 mm), the earth pressure acting on the upper portion of the 2RP (400 mm-700 mm BGS) reached the Coulomb active pressure. This occurred because the upper portion of the bench zone was a relaxation zone, as discussed in Section 4.1.2. In addition, because B was small, the value of σ_{p1} acting on the upper portion of the 2RP (400 mm-700 mm BGS) was close to σ_{a2} at the same depth, which also approached the Coulomb active pressure. On the other hand, the lower portion of the bench zone (700 mm-900 mm BGS) was a compaction zone (Fig. 9(a)). Therefore, the earth pressures acting on the lower portions of both rows of piles rapidly increased. The boundary

between the compaction and relaxation zones was located at approximately 700 mm BGS, which matches the stress distribution in Fig. 11.

Generally, because B is limited, the earth pressures exerted by the bench zone on the 1RP and 2RP (i.e., σ_{p1} and σ_{a2}, respectively) tend to be close together at every excavation depth during the second excavation phase.

5.2.2 Influence of the bench width on the earth pressure distribution

The influence of B can be obtained by comparing the earth pressures in M1, M2 and M3. The earth pressures shown in Fig. 12 indicate that σ_{p1} in M2 was smaller than that in M1 at the end of the first excavation phase (400 mm). This result occurred because B was larger in M2 than in M1 even though both bench zones were compaction zones; however, the compaction ratio of the bench zone in M2 was smaller than that in M1, as discussed in Section 4.1.2. Therefore, the 2RP had less influence on restraining the bench zone and the development of the passive earth pressure.

At the critical state of the excavation in M2 (i.e., an excavation depth of 725 mm), σ_{a2} was close to the Coulomb active pressure. Because B was larger in M2, the rotation of the 2RP in M2 had less influence on σ_{p1} than that in M1. Consequently, the upper portion of σ_{p1} in M2 was much larger than that in M1 and was not as close to the Coulomb active pressure as the upper portion of σ_{a2}. Correspondingly, the lower portion of σ_{p1} decreased compared to that in M1 to maintain the equilibrium of the 1RP. On the other hand, the distribution of σ_{p1} in M2 was triangular, which was quite different from that in M1. The lower portion of the bench zone was a compaction zone. However, because B was larger in M2, the compaction ratio was smaller. Therefore, the lower portion of σ_{a2} in M2 was smaller than that of M1. As B increased, the difference between σ_{p1} and σ_{a2} increased in M2.

Fig. 13 shows that σ_{p1} and σ_{a2} in M3 were much smaller than those in M1 at the end of the first excavation phase, further confirming that the restraint effect on the bench zone provided by the 2RP decreases with increasing B. At the critical state (i.e., an excavation depth of 750 mm), σ_{a2} had a distribution that matched the earth pressures for an unpropped wall, as proposed by Bolton and Powrie (1988). This result indicates that the 2RP can rotate independently and were not significantly affected by the 1RP. However, although B was relatively large, the deformation of 1RP was still affected by the rotation of the 2RP, as shown in Fig. 9(c). As the excavation depth increased, the rotation angle of the 2RP increased; thus, the displacement of the 1RP increased. Therefore, σ_{a1} decreased and approached the active state, and σ_{p1} decreased correspondingly.

In summary, the difference between σ_{p1} and σ_{a2} increased as B increased, indicating that the interaction between the two rows of piles decreased. When B was small (100 mm), σ_{p1} and σ_{a2} were close and both differed considerably from the conventional distributions. However, when the bench was sufficiently wide (B=400 mm), the 2RP could rotate independently, and σ_{a2} had a pattern similar to that of a normal single-row cantilever pile. However, the deformation and earth pressure of the 1RP were still influenced by the deformation of the 2RP.

5.2.3 Influence of the length of the 2RP on the earth pressure distribution

The earth pressures in the model with long 2RP (700 mm) are shown in Fig. 14. The earth pressure distributions of σ_{p1} and σ_{a2} in M4 were similar to those of M1 at the end of the first excavation phase. In the second excavation phase, the earth pressure distributions of σ_{p1} and σ_{a2} in M4 differed considerably from those in M1, which were larger in the upper portion of the bench zone and lower in the lower portion of the bench zone. At the critical excavation depth (i.e., 725 mm), the distribution of σ_{a2} acting on the upper portion of the 2RP (400 mm-700 mm BGS) was

triangular, whereas σ_{a2} acting on the lower portion of the 2RP (700 mm-1000 mm BGS) tended toward the Coulomb active pressure. The extremely large pressure near the toe of the 2RP (1000 mm-1100 mm BGS) implied that the 2RP rotated around a pivot point in the lower part of the pile. However, because B was small, σ_{p1} was close to σ_{a2} at the same elevation in M4, similar to M1.

For the second excavation phase, the difference between the earth pressure distributions in M1 and M4 was caused by the different locations of the compaction and relaxation zones, as shown in Fig. 9. For an excavation depth of 700 mm in M4, the locations of the compaction and relaxation zones (above and below 700 mm BGS) were in good agreement with the distributions of σ_{p1} and σ_{a2}. The earth pressures σ_{p1} and σ_{a2} approached the active pressure in the relaxation zone (700 mm-1000 mm BGS) but were relatively large in the compaction zone (400 mm-700 mm BGS). Further parametric studies showed that the distribution pattern of the earth pressure changed when the position of the pile toe of the 2RP became lower than that of the 1RP.

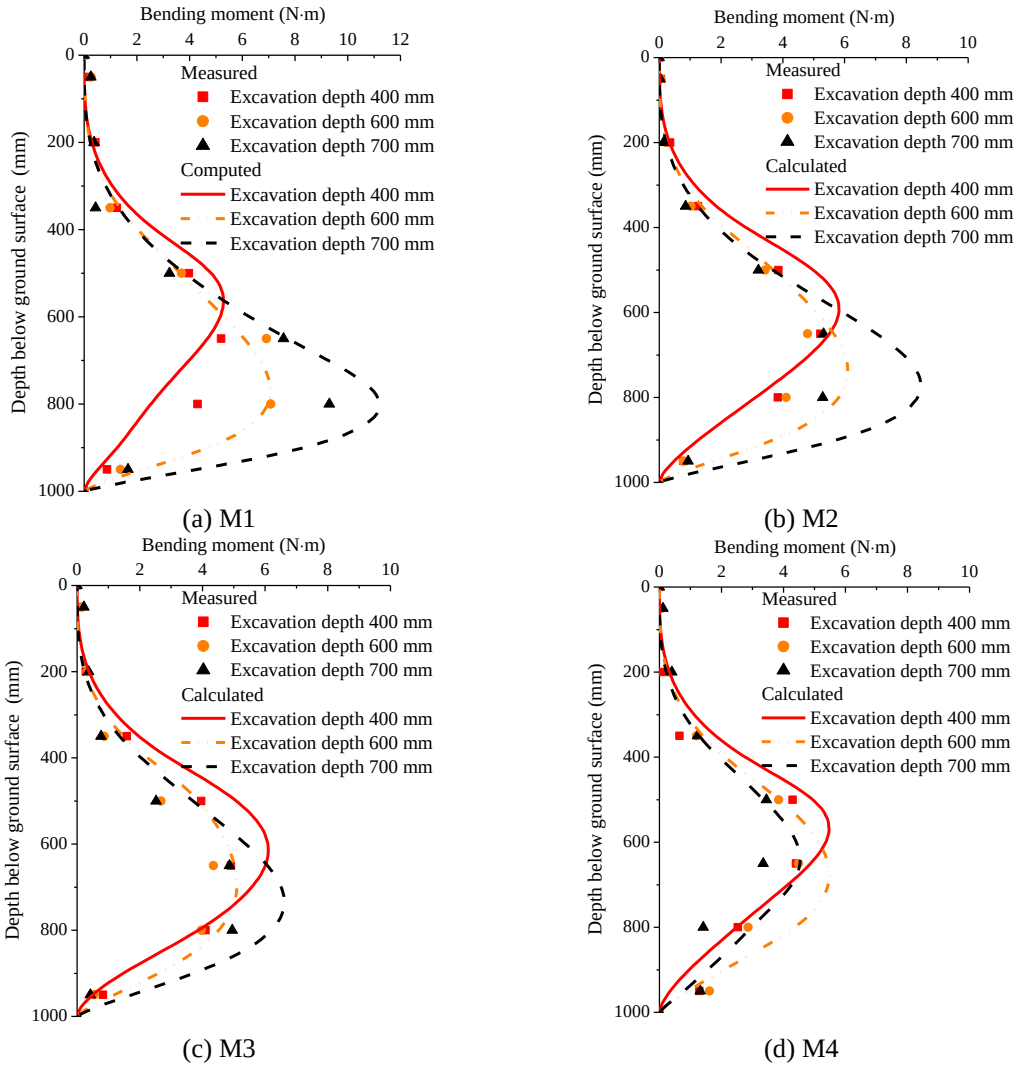

Fig. 15 Bending moment of the 1RP

5.3 Bending moment

As shown in Fig. 15, as the excavation depth increased in each test, the calculated bending moments of the 1RP had the same variation tendencies as the test results; however, some calculated values were slightly larger. Comparing the bending moments in the experimental and numerical simulations further verified the accuracy of the FDM simulation and the model test. Because the numerical simulation had more results than the model tests, the discussion below is based on the calculated results.

5.3.1 Influence of the bench width on the bending moment

(1) Bending moment in the 1RP at the end of the first excavation phase

Fig. 16 shows the values and positions of the maximum bending moments of the 1RP in M1-M4 and those in the single-row pile model. When the first excavation phase was completed (i.e., an excavation depth of 400 mm), the maximum bending moments in the 1RP in all cases were similar. However, the slight differences between these values exhibited a notable feature: a larger B led to a larger maximum bending moment. This finding can be explained by the difference between the net earth pressures acting on the 1RP in different tests (derived from Figs. 11-13), as shown in Fig. 17.

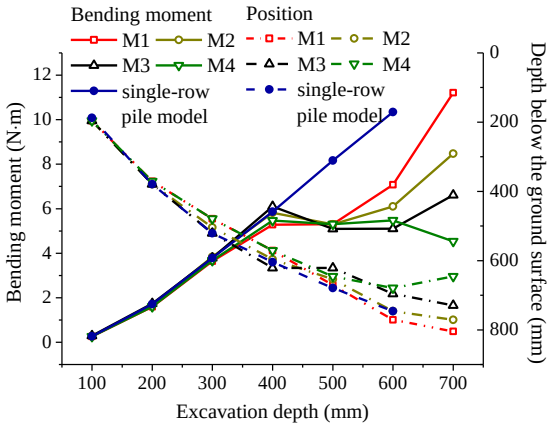

Fig. 16 Value and position of the maximum bending moment in the 1RP

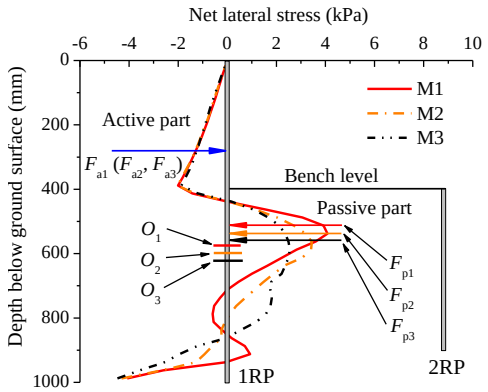

Fig. 17 Net lateral earth pressures acting on the 1RP for an excavation depth of 400 mm

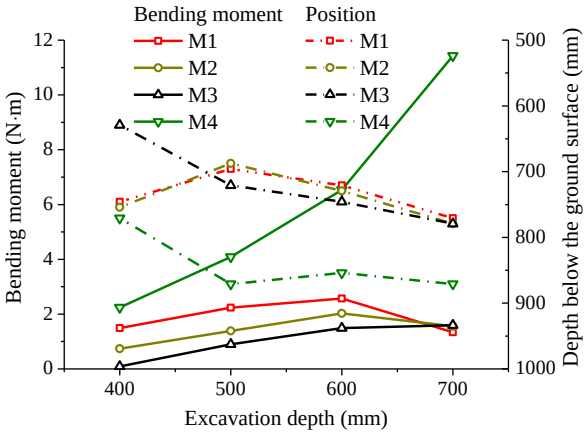

Fig. 18 Maximum bending moment in the 2RP

As discussed in Section 4.2.2, for an excavation depth of 400 mm, the values and distributions of σ_{a1} in M1-M3 were similar; however, the upper part of σ_{p1} decreased as B increased. Consequently, the position where the shear force in the pile was zero (O_1, O_2 and O_3 for M1, M2 and M3, respectively), which is also the position where the bending moment in the pile was the largest, became lower with increasing B, as shown in Fig. 17. The net earth pressures in the 1RP above the zero shear force point in each test can be divided into two parts according to their direction; for convenience, these parts are called the active part and passive part, as shown in Fig. 17.

The resultant forces of the earth pressures in the active parts of M1, M2 and M3, i.e., F_{a1}, F_{a2} and F_{a3}, respectively, had approximately the same values and action points. The resultant forces of the earth pressures in the passive parts of M1, M2 and M3, i.e., F_{p1}, F_{p2} and F_{p3}, respectively, also had the same values, but the action point became lower with increasing B. Therefore, the bending moment at the point of zero shear force (i.e., the maximum bending moment in the 1RP) caused by the resultant forces of the earth pressures in the active part and passive part increased with increasing B.

The above analysis shows that, in general, when σ_{a1} does not change significantly and the upper portion of σ_{p1} decreases, the point of zero shear force and maximum bending moment will be lower, and the maximum bending moment will increase. This conclusion is used in the following discussion.

(2) Bending moment in the 1RP during the second excavation phase

As shown in Fig. 16, during the second excavation phase, the difference between the bending moments of these tests gradually increased. The bending moments in the 1RP in M1-M4 were much smaller than that of the single-row pile model. Specifically, the bending moments in the 1RP for M1-M4 were 31.6%, 41%, 50.7% and 47.1% smaller than that of the single-row pile model at an excavation depth of 600 mm.

In M1, the maximum bending moment in the 1RP generally increased with increasing excavation depth, whereas the bending moments in M2 and M3 first decreased (at the excavation depth of 500 mm) and then increased. For M1, the upper portion of σ_{p1} was relatively large at the end of the first excavation phase. However, when the second excavation phase began, the upper portion of σ_{p1} decreased significantly. Therefore, the position of the maximum bending moment

moved downward during the entire second excavation phase, and the maximum bending moment increased gradually, as shown in Fig. 16. For M2 at an excavation depth of 500 mm, although σ_{p1} decreased to a certain level, the decrease in σ_{a1} was dominant; therefore, the maximum bending moment decreased slightly. For M3 at an excavation depth of 500 mm, the change in the maximum bending moment was similar to that in M2.

For M2 and M3, when the excavation depth was greater than 500 mm, the decrease in the upper portion of σ_{p1} became dominant again. Consequently, their maximum bending moments began to increase, and the position of the maximum bending moment began to move downward. For the excavation depths of 600 mm and 700 mm, when *B* increased, the maximum bending moment decreased, unlike for the excavation depth of 400 mm. For example, the maximum bending moment in M3 decreased 41% compared with that in M1 at the excavation depth of 700 mm. This difference is due to the values and distributions of the upper portion of σ_{a1} in M1-M3 remaining close for excavation depths of 600 mm and 700 mm, while the upper part of σ_{p1} increased with increasing *B*.

In the second excavation phase, the changing rate of the maximum bending moment in the 1RP and its position decreased with increasing *B* and was much smaller than that of the single-row pile model. Therefore, with increasing *B*, the second excavation has less impact on the bending moment of the 1RP.

(3) Bending moment in the 2RP

The bending moment of the 2RP for each case is shown in Fig. 18. At the end of the first excavation phase (400 mm), although the 2RP were totally embedded, the bending moments in the 2RP in M1 and M2 were not very small because of the influence of the 1RP. For excavation depths of 400-600 mm, the maximum bending moment in the 2RP increased with decreasing *B* because the upper portion of σ_{a2} increased with decreasing *B*. As the excavation depth increased, the bending moment of the 2RP first increased and then decreased in M1 and M2; however, this decrease was not observed in M3. For an excavation depth of 700 mm, the upper portion of σ_{a2} in the relaxation zone decreased significantly in the second excavation phase, but the decrease in M3 was smaller than those in M1 and M2. Regardless, the increasing rate of the bending moment in M3 decreased.

In summary, *B* can significantly influence the variations of the bending moments in the 1RP and 2RP through its influence on the earth pressure distributions in the bench zone. For the two-bench retained excavations in which the bottom of the 2RP is shallower than that of the 1RP (such as M1-M3), when *B* was small, the bending moment in 1RP increased rapidly during the second excavation phase; however, when *B* was large, the bending moment in 1RP changed only slightly. The bending moment in the 2RP was very small compared with that in the 1RP, which indicates that for the 2RP in this system, the pile strength can be relatively low or the pile space can be relatively large; therefore, installing the 2RP is not very costly.

5.3.2 Influence of the length of the 2RP on the bending moment

Figs. 15(d) and 16 show that the maximum bending moment of the 1RP in M4 remained approximately constant when the excavation depth was shallower than 600 mm in the second excavation phase; after this point, the maximum bending moment decreased slightly. The reason for this is that as the excavation depth increased, the upper portion of σ_{p1} was in the compaction zone and did not decease significantly, unlike in M1. Therefore, as shown in Fig. 16, the maximum bending moments in the 1RP in M4 were much smaller than those in M1 in the second excavation phase. In contrast, the bending moments of the 2RP in M4 were much larger than those in M1

(Fig. 18) because the upper portion of σ_{a2} was in the compaction zone. Furthermore, the compaction zone in M4 was much larger than that in M1, particularly at excavation depths of 600 and 700 mm.

When the 2RP was longer, it experienced a larger bending moment; thus, the bending moment in the 1RP decreased. Varying L_2 could redistribute the bending moments in the two rows of piles. For example, the 1RP experienced 89.3% of the total bending moments of the 1RP and 2RP (i.e., the total bending moment) in M1, but it experienced 28.4% of the sum bending moment in M4 at an excavation depth of 700 mm. The difference between the bending moments of M1 and M4 was fundamentally caused by the different deformation modes of the 1RP and 2RP.

5.4 Failure mechanism

In conventional geotechnical engineering, defining a failure mechanism is the basis for establishing the stability analysis (Cheng *et al*. 2015). To evaluate the stability of an excavation, a slip surface typically needs to be assumed; calculations using different slip surfaces may derive completely distinct stability factors. Therefore, assuming a reasonable slip surface is a crucial factor for stability evaluations. The failure mechanism of the multi-bench system is studied in this section.

5.4.1 General description

Figs. 19-22 show the contours of the maximum shear strain rate in the numerical models at the critical excavation depths and pictures of the failure scenarios in the model tests.

As shown in Figs. 19-22, shear bands can be observed in the contours of the maximum shear strain rate in all of the tests. These shear bands all have larger inclined angles with respect to the z-axis (vertical axis) than that of the Coulomb slip surface obtained from the critical internal friction angle (31°). In the photographs of the model tests, the solid red lines represent the observed slip surfaces. In the tests, all the observed slip surfaces had smaller inclined angles with respect to the vertical axis than that of the Coulomb slip surface. In addition, these slip surfaces were not as close to the pile toes as those in the numerical simulations. The above problems in the model tests could be primarily caused by the friction between the toughened glass window and the sand.

Although there were slight differences among the slip surfaces obtained from the model tests, numerical simulations and Coulomb's theory, in general, the calculated and experimental test results reflect the failure mechanism of the two-bench retaining systems.

5.4.2 Influence of the bench width on the failure mechanism

As shown in Fig. 19, in the numerical simulation, the retaining system reached the critical state at an excavation depth of 700 mm in M1. The slip surfaces were formed on the retained side of the excavation, and there was not an obvious shear band or slip surface in the bench zone soil. In addition, the photograph of the failed model shows that the rotation angle of the 1RP (3.25°) was slightly smaller than that of the 2RP (4.21°), which is consistent with the calculated results shown in Fig. 9(a).

As shown in Fig. 20, the critical excavation depth derived in the numerical simulation was 725 mm in M2, which implies better stability than that in M1. In the model test, as shown in Fig. 20(b), slip surfaces can be observed in the soil on the retained side and in the bench zone. Two slip surfaces were formed in the soil in the bench zone, with the longer one running from the toe of the 2RP to the intersection of the bench level and the 1RP. At the critical state of the numerical model,

as shown in Fig. 20(a), the main shear band was formed on the retained side, and certain discontinuous shear bands can be observed in the bench zone.

Fig. 21 shows the failure mechanism for M3, for which the calculated critical excavation depth was 750 mm. In Fig. 21(b), slip surfaces were formed in the bench zone, and no obvious shear band occurred on the retained side of the 1RP. Similar failure modes can be observed in the calculated critical state of the numerical model except for a short shear band with a small shear strain rate on the retained side of the 1RP.

The effect of *B* on the failure mechanism can be summarized based on the above analysis. The stability of a two-bench retaining system increases with *B* because the critical excavation depth increases with increasing *B*. Additionally, three completely different failure mechanisms were observed in M1, M2 and M3.

In M1, the failure of the 1RP and 2RP occurred simultaneously, and the slip surfaces developed outside the retaining system (i.e., the two rows of the retaining piles and the soil between them). Based on the discussion in Sections 4.1 and 4.2, the earth pressures acting on the 1RP and 2RP exerted by the bench zone soil (Fig. 11) showed high consistency, and the movements of the two levels of piles also exhibited relatively high compatibility (Fig. 19). Both of these results imply the concurrent collapse of the 1RP and 2RP. A slip surface was not formed in the bench zone, and the failure mode of the entire retaining system was similar to that of an unpropped retaining wall. Therefore, this failure mode can be defined as “integrated failure”.

In M2, the two levels of piles both failed, but not with an integrated failure, such as that in M1. As the excavation proceeded on the excavated side of the 2RP, overturning failure of the 2RP occurred first, followed by the failure of the 1RP. The interaction between the 1RP and 2RP and the integrity of the retaining system was much smaller than that in M1. The slip surfaces caused by the failure of the 2RP were formed in the bench zone. Because the bench zone was not sufficiently wide, the slip surfaces extended to the 1RP, thus influencing the stability of the 1RP. This failure mode is defined as “interactive failure”.

In M3, the interaction between the 1RP and 2RP became even smaller. The failure of one level of piles did not lead to the failure of the other one. In test M3, as the excavation depth increased, the 2RP failed while the 1RP remained stable. This failure mode can be defined as “disconnected failure”.

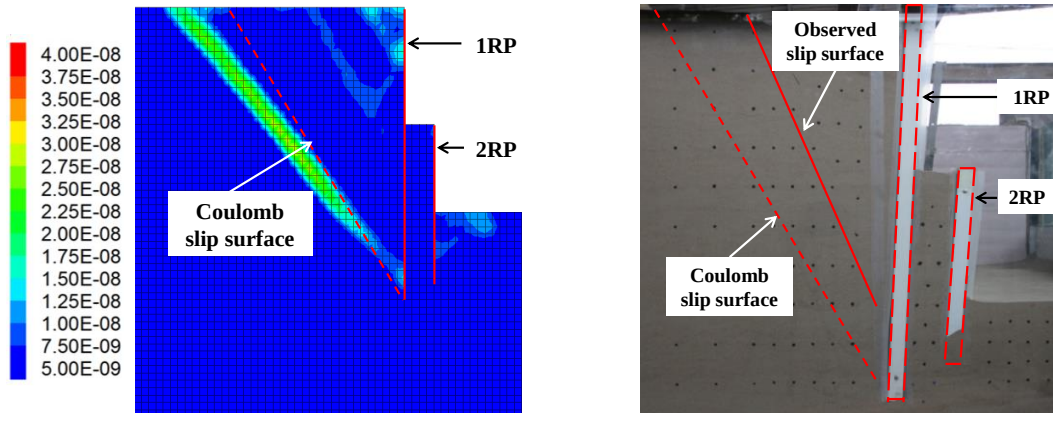

(a) Shear strain rate of the FDM model at the critical depth (b) Photograph of the failed model

Fig. 19 Failure mechanism of M1

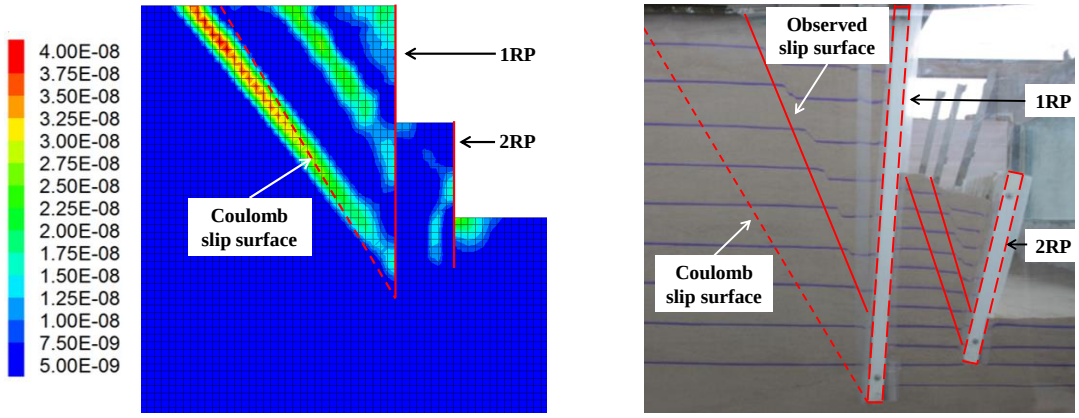

(a) Shear strain rate of the FDM model at the critical depth (b) Photograph of the failed model

Fig. 20 Failure mechanism of M2

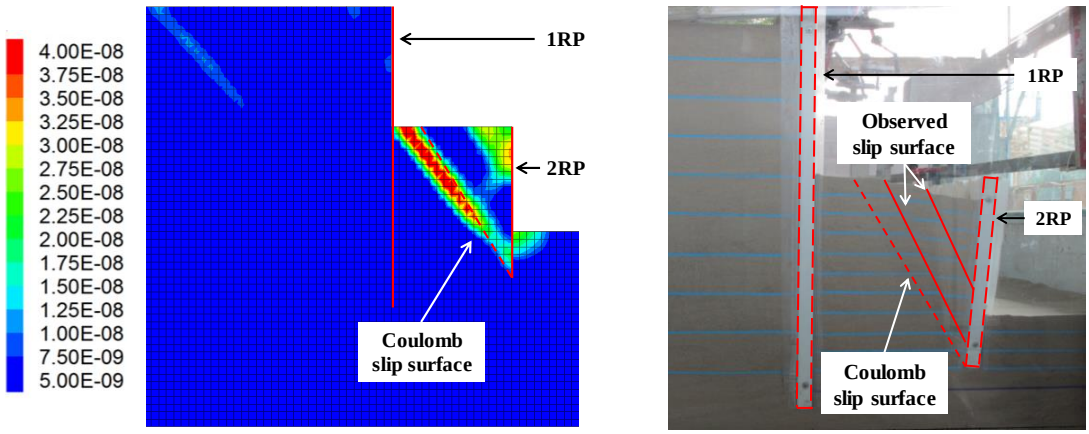

(a) Shear strain rate of the FDM model at the critical depth (b) Photograph of the failed model

Fig. 21 Failure mechanism of M3

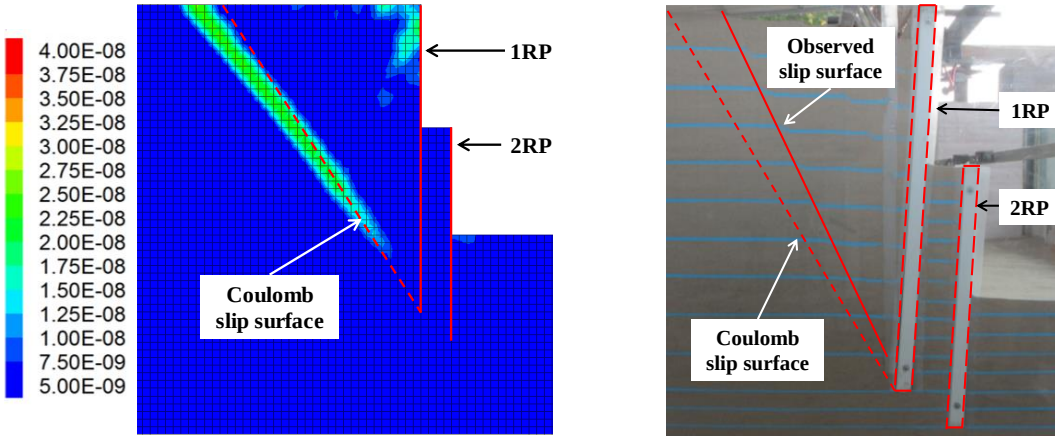

(a) Shear strain rate of the FDM model at the critical depth (b) Photograph of the failed model

Fig. 22 Failure mechanism of M4

5.4.3 Influence of the length of the 2RP on the failure mechanism

Fig. 22 shows the failure mechanism of M4. The calculated critical excavation depth is 750 mm in this case, which indicates that the excavation stability was greatly improved with increasing L_2. M4 has the same failure mechanism as M1 (integrated failure). The photo of the failed model shows that the rotation angle of the 1RP (6.98°) was larger than that of the 2RP (6.16°), which is consistent with the calculated results in Fig. 9(d) but differs from that in M1, as shown in Fig. 19(b).

6. Conclusions

Multi-bench retaining systems are economical and time saving for large excavation projects. Four model tests were conducted to study the working and failure mechanisms of a multi-bench retaining system. Finite difference models considering the hardening and softening characteristics of sand were established to simulate and verify the model tests and to obtain more results. Based on the analysis of the test and numerical results, the following conclusions, which provide a reference for the design of this type of retaining system, can be derived:

(1) Compared with the excavation retained using a cantilever pile (i.e., a single-row pile), the multi-bench retained excavation has smaller displacement and bending moment and larger stability for the same excavation depth. For instance, at an excavation depth of 600 mm, the horizontal displacement and bending moment in M1 were 22.6% and 31.6% smaller than those of the single-row pile model, respectively, and the ultimate excavation depth of the multi-bench retained excavation was much larger than that of the single-row pile model. Compared with a berm-supported retaining system, the multi-bench retaining system needs less space and is suitable for a deeper excavation depth. Additionally, compared with a retaining system with horizontal struts, the multi-bench retaining system is more economical and time saving.

(2) Adding the 2RP decreases the displacement of the 1RP. When B increased from 100 mm to 400 mm, the displacement of the 1RP decreased by up to 69.3%; when L_2 increased from 500 mm to 700 mm, the displacement of the 1RP decreased by up to 46.5%. The soil between the two rows of piles can be divided into compaction and relaxation zones based on the relative movement between the 1RP and 2RP at the same elevation, which is primarily determined by their embedded pile lengths. For a small L_2, the relaxation zone is located at the upper portion of the bench zone, whereas for a large L_2, the relaxation zone is located at the lower portion. In addition, the compaction or relaxation ratios decrease with increasing bench zone width.

(3) The horizontal stress distribution in the bench zone is significantly affected by the compacted or relaxed state of the soil (i.e., the relative movement between the two rows of piles). The differences in the earth pressures exerted by the bench zone on the 1RP and 2RP (i.e., σ_{p1} and σ_{a2}) increased with increasing B. When B was small, σ_{p1} and σ_{a2} were close and both differed considerably from the conventional distributions. However, when the bench was sufficiently wide, σ_{a2} had a similar pattern to that of a normal single-row cantilever pile. For an excavation with short 2RP, the upper parts of σ_{p1} and σ_{a2} are close to the Coulomb active pressure, whereas for an excavation with long 2RP, the lower parts of σ_{p1} and σ_{a2} are close to the Coulomb active pressure. The changes in the earth pressure distributions were caused by the varying locations of the compaction and relaxation zones, as discussed in Conclusion (2).

(4) B and L_2 can significantly influence the distribution of the bending moments in the 1RP and 2RP through their influence on the earth pressure distributions in the bench zone. For the same

excavation depth during the first excavation phase, the bending moment in the 1RP is slightly larger when B is larger, whereas in the second excavation phase, the bending moment in the 1RP is much smaller when B is larger. Specifically, the bending moment in the 1RP decreased 59.6% when B increased from 100 mm to 400 mm. When the bottom of the 2RP was shallower than the bottom of the 1RP, the 1RP accounted for 89.3% of the total bending moment in the retaining system in M1. Thus, in this case, the bending moment in the 2RP was very small, implying that installing the 2RP is not very costly. When L_2 increases from 500 mm to 700 mm, the 2RP will experience a larger bending moment, even larger than that in the 1RP, and the 2RP accounted for 71.6% of the total bending moment in M4.

(5) The stability of a multi-bench retaining system increases with increasing B and L_2. For different values of B, three different failure mechanisms were observed in the model tests and numerical simulations. For the integrated failure, slip surfaces cannot be formed in the bench zone; for the interactive failure, slip surfaces developed in the bench zone and influenced the stability of the 1RP; and for the disconnected failure, the slip surfaces for the failure of the 1RP and 2RP formed separately.

Acknowledgments

This work was supported by the Tianjin Research Program of Application Foundation and Advanced Technology (Grant No. 14CQNJC07500), the China Postdoctoral Science Foundation (Grant No. 2014M561186), and the National Natural Science Foundation of China (Grant No. 51508382 and 51308389). Their support is gratefully acknowledged.

References

Anastasopoulos, I., Gazetas, G., Bransby, M.F., Davies, M.C.R. and El Nahas, A. (2007), "Fault rupture propagation through sand: Finite-element analysis and validation through centrifuge experiments", *J. Geotech. Geoenviron. Eng.*, **133**(8), 943-958.

Ardakani, A., Bayat, M. and Javanmard, M. (2014), "Numerical modeling of soil nail walls considering mohr coulomb, hardening soil and hardening soil with small-strain stiffness effect models", *Geomech. Eng.*, **6**(4), 391-401.

Bildik, S. and Laman, M. (2015), "Experimental investigation of the effects of pipe location on the bearing capacity", *Geomech. Eng.*, **8**(2), 221-235.

Bolton, M.D. and Powrie, W. (1987), "The collapse of diaphragm walls retaining clay", *Geotechnique*, **37**(3), 335-353.

Bolton, M.D. and Powrie, W. (1988), "Behaviour of diaphragm walls in clay prior to collapse", *Geotechnique*, **38**(2), 167-189.

Carder, D.R. and Bennett, S.N. (1996), *The Effectiveness of Berms and Raked Props as Temporary Support to Retaining Walls*, TRL Rep. 213.

Cheng, X., Zheng, G., Soga, K., Bandara, S.S., Kumar, K., Diao, Y. and Xu, J. (2015), "Post-failure behavior of tunnel heading collapse by MPM simulation", *Sci. China Technol. Sci.*, **58**(12), 2139-2152.

Clough, G.W. and Davidson, R.R. (1977), "Effects of construction on geotechnical performance", *Proceedings of the 9th International Conference Soil Mechanics and Foundation Engineering*, Specialty Session III, Tokyo, July.

Daly, M.P. and Powrie, W. (2001), "Undrained analysis of earth berms as temporary supports for embedded retaining walls", *Proc. Inst. Civ. Eng. Geotech. Eng.*, **149**(4), 237-248.

Desai, C.S. and Ma, Y. (1992), "Modelling of joints and interfaces using the disturbed-state concept", *J. Numer. Anal. Meth. Geomech.*, **16**(9), 623-653.
Do, N.A., Dias, D. and Oreste, P. (2013a), "3D modelling for mechanized tunnelling in soft ground-influence of the constitutive model", *Am. J. Appl. Sci.*, **10**(8), 863-875.
Do, N.A., Dias, D., Oreste, P.P. and Djeran-Maigre, I. (2013b), "2D numerical investigations of twin tunnel interaction", *Geomech. Eng.*, **6**(3), 263-275.
Fan, C. and Fang, Y. (2010), "Numerical solution of active earth pressures on rigid retaining walls built near rock faces", *Comput. Geotech.*, **37**(7), 1023-1029.
Frydman, S. and Keissar, I. (1987), "Earth pressure on retaining walls near rock faces", *J. Geotech. Eng.*, **113**(6), 586-599.
Georgiadis, M. and Anagnostopoulos, C. (1998), "Effect of berms on sheet-pile wall behaviour", *Geotechnique*, **48**(4), 569-574.
Gourvenec, S.M. and Powrie, W. (2000), "Three-dimensional finite element analyses of embedded retaining walls supported by discontinuous earth berms", *Can. Geotech. J.*, **37**(5), 1062-1077.
Greco, V. (2013), "Active thrust on retaining walls of narrow backfill width", *Comput. Geotech.*, **50**, 66-78.
Hong, Y. and Ng, C.W.W. (2013), "Base stability of multi-propped excavations in soft clay subjected to hydraulic uplift", *Can. Geotech. J.*, **50**(2), 153-164.
Itasca Consulting Group (2009), "FLAC fast Lagrangian analysis of continua, version 5.0, User's manual.
Jewell, R.A. (1989), "Direct shear tests on sand", *Geotechnique*, **39**(2), 309-322.
Kim, C., Kwon, J., Im, J.C. and Hwang, S. (2012), "A method for analyzing the self-supported earth-retaining structure using stabilizing piles", *Mar. Georesour. Geotec.*, **30**(4), 313-332.
Lee, C., Wei, Y., Chen, H., Chang, Y., Lin, Y. and Huang, W. (2011), "Stability analysis of cantilever double soldier-piled walls in sandy soil", *J. Chin. Inst. Eng.*, **34**(4), 449-465.
Liao, H.J. and Lin, C.C. (2009), "Case studies on bermed excavation in Taipei silty soil", *Can. Geotech. J.*, **46**(8), 889-902.
Ouria, A., Toufigh, V., Desai, C. and Toufigh, V. (2016), "Finite element analysis of a CFRP reinforced retaining wall", *Geomech. Eng.*, **10**(6), 757-774.
Park, J., Joo, Y. and Kim, N. (2009), "New earth retention system with prestressed wales in an urban excavation", *J. Geotech. Geoenviron. Eng.*, **135**(11), 1596-1604.
Peck, R.B. (1969), "Deep excavations and tunneling in soft ground", *Proceedings of the 7th International Conference on SMFE*, Mexico City.
Pietruszczak, S. and Mróz, Z. (1981), "Finite element analysis of deformation of strain-softening materials", *J. Numer. Meth. Eng.*, **17**(3), 327-334.
Potts, D.M., Addenbrooke, T.I. and Day, R.A. (1993), *The Use of Soil Berms for Temporary Support of Retaining Walls*, Thomas Telford, London, U.K.
Powrie, W. and Daly, M.P. (2002), "Centrifuge model tests on embedded retaining walls supported by earth berms", *Geotechnique*, **52**(2), 89-106.
Qu, H., Li, R., Hu, H., Jia, H. and Zhang, J. (2016), "An approach of seismic design for sheet pile retaining wall based on capacity spectrum method", *Geomech. Eng.*, **11**(2), 303-323.
Seo, M., Im, J., Kim, C. and Yoo, J. (2016), "Study on the applicability of a retaining wall using batter piles in clay", *Can. Geotech. J.*, **53**(8), 1195-1212.
Take, W.A. and Valsangkar, A.J. (2001), "Earth pressures on unyielding retaining walls of narrow backfill width", *Can. Geotech. J.*, **38**(6), 1220-1230.
Tatsuoka, F., Sakamoto, M., Kawamura, T. and Fukushima, S. (1986), "Strength and deformation characteristics of sand in plane strain compression at extremely low pressures", *Soils Found.*, **26**(1), 65-84.
Toufigh, V., Desai, C.S., Saadatmanesh, H., Toufigh, V., Ahmari, S. and Kabiri, E. (2014), "Constitutive modeling and testing of interface between backfill soil and fiber-reinforced polymer", *J. Geomech.*, **14**(3), 04014009.
Toufigh, V., Masoud Shirkhorshidi, S. and Hosseinali, M. (2016), "Experimental investigation and constitutive modeling of polymer concrete and sand interface", *J. Geomech.*, **17**(1), 04016043.

Vardoulakis, I. and Graf, B. (1985), "Calibration of constitutive models for granular materials using data from biaxial experiments", *Geotechnique*, **35**(3), 299-317.
Yang, K.H. and Liu, C.N. (2007), "Finite element analysis of earth pressures for narrow retaining walls", *J. GeoEng*., **2**(2), 43-52.
Yang, M., Chen, S. and Chen, S. (2006), "Innovative central opening strut system for foundation excavation", *J. Constr. Eng. M.*, **132**(1), 58-66.
Zhao, Q. and Zhu, J.M. (2014), "Research on active earth pressure behind retaining wall adjacent to existing basements exterior wall considering soil arching effects", *Rock Soil Mech*., **35**(3), 723-728.

CC